RSC Advances

PAPER

View Article Online
View Journal | View Issue

Cite this: *RSC Adv.*, 2024, **14**, 9594

Chitosan-induced $NH_4V_4O_{10}$ hierarchical hybrids as high-capacity cathode for aqueous zinc ion batteries

Yaotong Li,[a] Chunru Zhao,[a] Abdukayum Abdukader *[b] and Xiang Wu *[a]

Received 13th March 2024
Accepted 19th March 2024

DOI: 10.1039/d4ra01916d

rsc.li/rsc-advances

Aqueous zinc ion batteries (AZIBs) have been widely investigated due to their characteristics of convenient operation and intrinsic safety. However, there are several issues to be addressed in AZIBs, such as slow diffusion kinetics of Zn^{2+}, cathode material dissolution and the dendrite formation of zinc anodes. Thus, it is challenging to prepare a high-performance cathode material. In this work, we prepare $NH_4V_4O_{10}$ flower-like structures by a facile hydrothermal route. The introduction of chitosan significantly enlarges the layer spacing of the (001) crystal plane. The assembled Zn//NVO-0.15C batteries deliver a specific capacity of 520.54 mA h g^{-1} at a current density of 0.2 A g^{-1}. Furthermore, they maintain 91% of the retention rate at 5.0 A g^{-1} after 1000 times cycling. It demonstrates the excellent zinc ion storage behavior of ammonium vanadate electrode materials for AZIBs.

1. Introduction

In the past few years, the energy crisis and environmental pollution are globally worsened with the acceleration of industrialization. It motivates researchers to develop rechargeable energy storage devices to meet the increasing demands.[1,2] Currently, lithium ion batteries (LIBs) dominate most of the battery market with their combination of high energy density and wide operating voltage. However, the safety issues are not negligible due to the use of organic liquid electrolytes and short circuits.[3–6] Thus, aqueous zinc-ion batteries (AZIBs) are considered as the alternatives to LIBs with their safety, environmental friendliness, low cost and high theoretical capacity.[7–9] It is still a challenge to design cathodes with high specific capacity and durable cycle life.[10–12]

Ammonium vanadate compounds are regarded as a promising cathode material with excellent specific capacity, light weight and superior rate performance.[13–15] But the dissolution of vanadium and the collapse of the layer structure decrease their capacity and cyclic life.[16] Several strategies are utilized to improve the performance of electrode materials including interlayer insertion,[17] nuclear-shell encapsulation[18] and the introduction of oxygen defects.[19] For example, Zhao *et al.* designed Ga-NHVO-0.5 cathodes with the capacity of 438.23 mA h g^{-1} at 0.2 A g^{-1}.[20] The addition of Ga increased the specific surface area of $(NH_4)_2V_{10}O_{25}\cdot 8H_2O$ materials, which enhanced the transfer of Zn^{2+}. Besides, Zhao and coworkers synthesized graphene oxide encapsulated VO_2 nanobelts.[21] The carbon layer improves the electrical conductivity and facilitates the insertion and de-insertion of Zn^{2+}. The cells deliver a capacity of 323 mA h g^{-1} at 0.1 A g^{-1}. Moreover, Peng *et al.* introduced oxygen defects into $NH_4V_4O_{10}$.[22] The oxygen vacancy reduces the diffusion barrier of Zn^{2+} and forms a stable crystal structure during cycling. The as-assembled batteries possess the specific capacity of 499 mA h g^{-1} at 0.2 A g^{-1} and a 95.1% retention at 5 A g^{-1} for 4000 times cycling. However, there is a lack of exploration and experiment with intercalated polymers of ammonium materials.

Herein, we introduce chitosan into $NH_4V_4O_{10}$ materials by a facile hydrothermal avenue. The synthesized products present a flower-like shape assembled by many nanorods/sheets, which provide abundant active sites during electrochemical reaction. The NVO-0.15C samples possess the specific surface area of 83.81 m^2 g^{-1}. The assembled Zn//NVO-0.15C batteries deliver a specific capacity of 520.54 mA h g^{-1} at 0.2 A g^{-1}. Also, they possess the energy density of 216.15 W h kg^{-1} at the power density of 450 W kg^{-1}. Meanwhile, the devices maintain 358.19 mA h g^{-1} at 5.0 A g^{-1} after 1000 times cycling.

2. Experimental section

2.1 Material synthesis

In the experiments, all the chemicals were directly used without any purification. The $NH_4V_4O_{10}$ samples were synthesized according to previous reports.[23] Firstly, 4 mmol NH_4VO_3 (99%, Shanghai Aladdin Corporation) and 4 mmol $H_2C_2O_4\cdot 2H_2O$ (99.5%, Tianjin Damao Corporation) were dissolved into 40 mL deionized water at 70 °C. Then, different

[a]School of Materials Science and Engineering, Shenyang University of Technology, Shenyang 110870, P. R. China. E-mail: wuxiang05@sut.edu.cn

[b]Xinjiang Key Laboratory of Novel Functional Materials Chemistry, College of Chemistry and Environmental Sciences, Kashi University, Kashi 844000, P. R. China. E-mail: abdukadera@sina.com

mass of chitosan (99.5%, Tianjin Damao Corporation) was added into the above solution under magnetic stirring. The mass of chitosan is 0.1, 0.15 and 0.2 g, respectively. The above mixture was then place in a water bath at a constant temperature of 70 °C. After stirring for 0.5 h, the precursor was removed and cooled to room temperature, the pH value of the solution was adjusted to 2 by adding four to five drops of 3 M hydrochloric acid. Then, the solution was transferred into 100 mL Teflon-lined autoclaves and putted in the electric oven. The mixture was heated at 180 °C for 24 h. After cooling to ambient temperature naturally, the products were centrifuged several times alternately with anhydrous ethanol and DI. Finally, the resulting precipitate was dried overnight in a desiccator at 60 °C. The collected black powder was labeled a NVO-0.1C, NVO-0.15C and NVO-0.2C, respectively. For comparison, pure $NH_4V_4O_{10}$ materials were also prepared without adding chitosan and labeled as NVO.

2.2 Structure and morphology characterization

The crystallographic and phase structure of the samples were evaluated by X-ray diffractometer (XRD, Rigaku Ultima IV, Cu Kα radiation, $\lambda = 0.1541$ nm, 40 kV). Then we utilized the X-ray photoelectron spectroscopy (XPS, Thermo fisher Nexsa G2) to characterize the valence of the elements. The morphology and microstructures of the products was observed by scanning electron microscope (SEM, Gemini, 300-71-31) and transmission electron microscope (TEM, JEOL JEM-F200). Finally, the specific surface area and pore size were characterized by the Brunauer–Emmett–Teller (BET) and Barrett–Joyner–Halenda (BJH) test system.

2.3 Electrochemical characterization

The cathode materials were fabricated by mixing the prepared samples, carbon black (Taiyuan Lizhiyuan Technology Corporation) and PVDF (polyvinylidene fluoride, Taiyuan Lizhiyuan Technology Corporation) with a mass ratio of 7 : 2:1. After that, an amount of *N*-methyl-L-2-pyrrolidone (NMP, 99%, Tianjin Damao Corporation) was added to the above mixture to form slurry, then applied on carbon paper. The carbon papers were made of 0.02 mm graphite foil. After that, it was dried in vacuum oven at 60 °C for 12 h. A series of CR2032-type cells were assembled with the obtained electrodes, glass fiber separators (Whatman), zinc foils (0.1 mm) and 3 M $Zn(CF_3SO_3)_2$ electrolyte (98%, Macklin Corporation). Before using, the zinc foils were sanded on both sides by using sandpapers and cut to 0.5 × 0.5 cm. Two fiberglass diaphragms were used as barriers between the positive and negative electrodes to stop short circuits caused by dendrites in the zinc anode. The mass average and thickness of the cathode are 1.4 mg and 0.2 mm, respectively. The automatic battery test system (Neware, CT-4008T-5 V6A-164) was employed to study the galvanostatic charge–discharge (GCD) curves and galvanostatic intermittent titration technique (GITT). Finally, we study the cyclic voltammetry (CV) and electrochemical impedance spectroscopy (EIS) by using an electrochemical workstation (CHI660E).

3. Results and discussion

Firstly, XRD is utilized to investigate the phase structures of the fabricated materials. As presented in Fig. 1a, the main characteristic peaks of the samples are well indexed to the $NH_4V_4O_{10}$

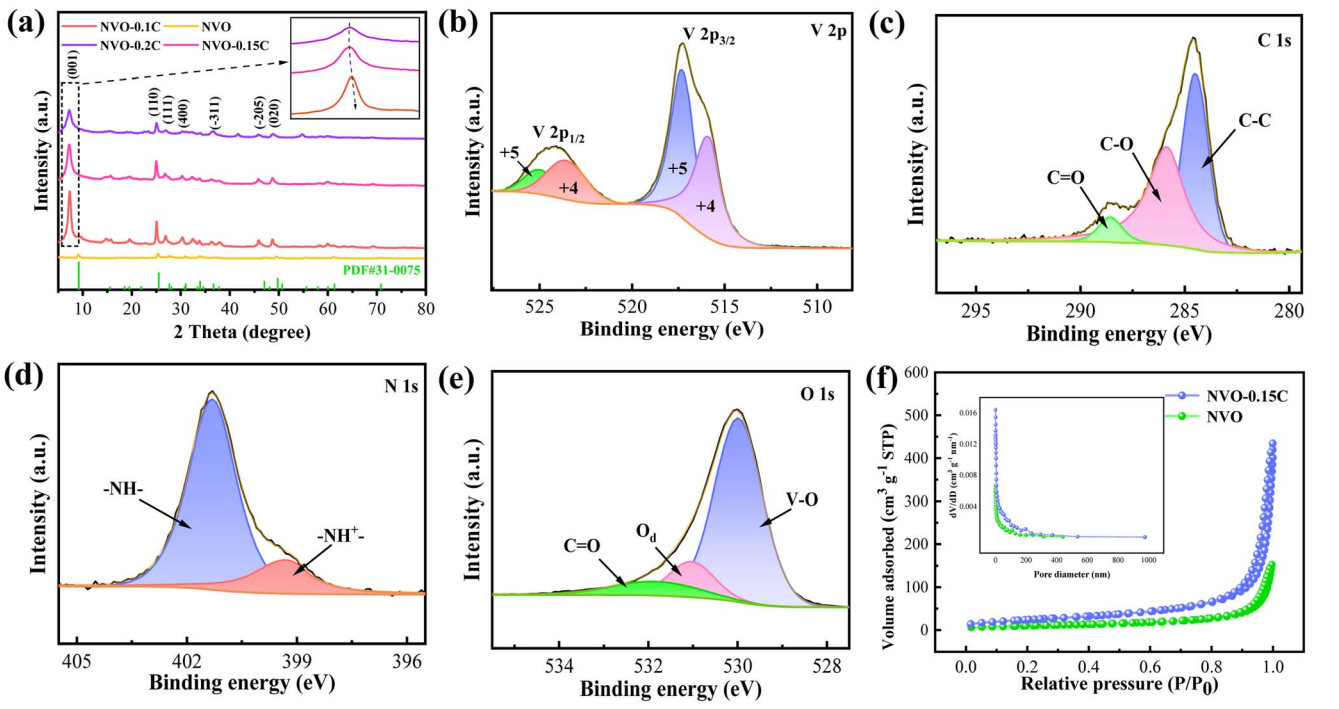

Fig. 1 Structure characterization (a) XRD patterns (b) V 2p (c) C 1s (d) N 1s (e) O 1s XPS spectra (f) N_2 adsorption–desorption isotherms and pore size distribution curve (insect) of the NVO and NVO–0.15C samples.

phase (PDF card No. 31-0075). The diffraction peaks at 9.2, 25.5, 27.7, 31.0, 33.9, 47.0 and 49.8° correspond to the (001), (110), (111), (400), (−311), (−205) and (020) crystal planes, respectively. It is worth noticeable that the (001) diffraction peaks shift to left significantly after chitosan adding, revealing the expansion of the interlayer spacing. The large layer spacing reduces the coulombic interactions when Zn^{2+} embedding, thus enhance the performance of NVO-0.1C and NVO-0.15C cathodes.[24] Moreover, there are slight difference in the characteristic peaks of chitosan doping samples, as shown in the enlarging pattern. The peaks of NVO-0.1C, NVO-0.15C and NVO-0.2C are located at 7.36, 7.26 and 7.28°, respectively. The slight rightward shift of the NVO-0.2C peak is attributed to the collapse of the layer structure, which leads to the degradation of the performance.[25]

Then we use XPS to characterize the chemical valence states and compositions of the samples. Fig. 1b shows the two distinct signal peaks of V $2p_{1/2}$ at 525.1/523.7 eV and V $2p_{3/2}$ at 517.3/516 eV, which belong to V^{5+} and V^{4+}, respectively.[26] The C 1s peak is fitted into three peaks, including C=O bond (288.6 eV), C–O bond (285.9 eV) and C–C bond (284.8 eV), as demonstrated in Fig. 1c.[27] The N 1s spectra corresponds two signal peaks located at 401.3 eV and 399.3 eV (Fig. 1d). They belong to neutral nitrogen (–NH–) and positively charged nitrogen ($–NH^+–$).[28] From Fig. 1e, the O 1s signal peaks at 530, 531.1 and 531.9 eV are assigned to the lattice oxygen (V–O), oxygen vacancy defects (O_d) and carbonyl group (C=O), respectively.[29] The N_2 adsorption–desorption isotherms of the products (Fig. 1f) indicate the typical type IV hysteresis loops, which suggest their mesoporous feature. The specific surface area of the NVO-0.15C materials (83.81 $m^2\ g^{-1}$) is larger than that of the NVO samples (35.35 $m^2\ g^{-1}$). Furthermore, the two samples possess the pore sizes of 0.453 and 0.296 $cm^3\ g^{-1}$, respectively. The high specific surface area and pore volume offer abundant active sites for the transfer of Zn^{2+} during electrochemical reaction.[30]

SEM is employed to observe the morphology of the samples. Compared with the NVO samples (Fig. 2a and b), the other two products (Fig. 2c–f) manifest flower-like shapes with the gradual

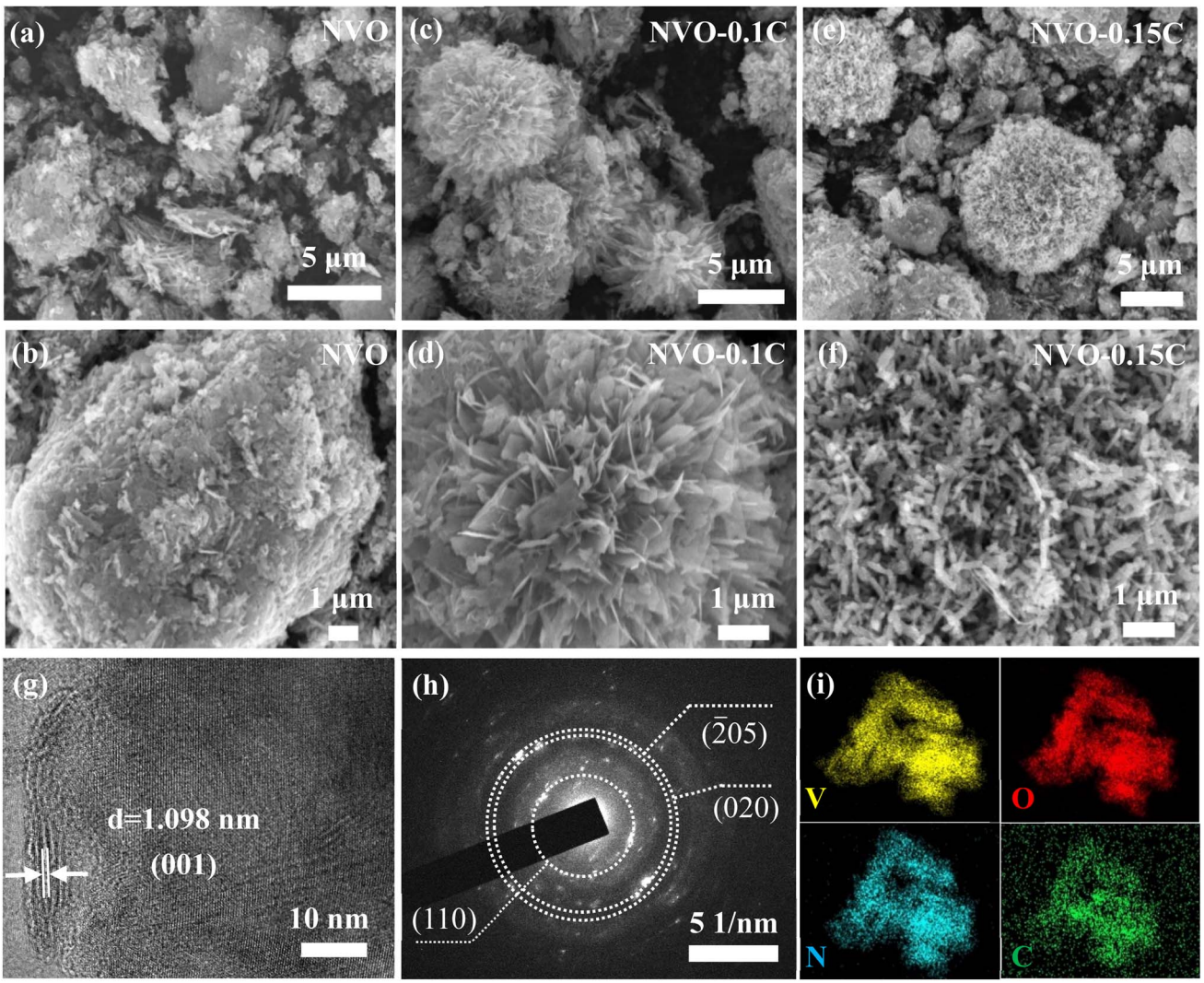

Fig. 2 Morphology characterization (a and b) SEM images of NVO (c and d) NVO-0.1C (e and f) NVO-0.15C samples (g) HRTEM images of NVO-0.15C sample (h) SAED pattern (i) the corresponding elements mapping images of NVO-0.15C sample.

addition of chitosan. Therefore, the morphology of vanadate samples is related to the addition of chitosan. As indicated in Fig. 2d, the NVO-0.1C powder consists of nanosheets. Similarly, many nanorods are interconnected and aggregated disorderly to form nanoflowers (Fig. 2f). Subsequently, Fig. 2g shows the HRTEM image of NVO-0.15C sample. The lattice fringe of 1.098 nm can be assigned to the (001) planes of NVO phase. It can be found that the layer spacing increases compared to that of the $NH_4V_4O_{10}$ (d(001) = 0.96 nm, PDF card no. 31-0075). This proves that the introduction of chitosan enlarges the crystal spacing of $NH_4V_4O_{10}$ sample, which is consist with the XRD results. Moreover, selected area electron diffraction (Fig. 2h) can be indexed to the (110), ($\bar{2}$05) and (020) planes of NVO-0.15C product, revealing that the fabricated sample belongs to typical polycrystalline structure. As shown in Fig. 2i, the uniform distribution of the elements (V, O, N, and C) is demonstrated by elemental mapping images, which proves the successful intercalation of chitosan.

To evaluate the electrochemical performance of the fabricated materials, many button batteries are assembled with 3 M $Zn(CF_3SO_3)_2$ electrolyte. Fig. 3a shows the first three cycles of the CV curves of NVO-0.15C cathode at the voltage ranging 0.2–1.6 V. The curve patterns are closely overlapping when the scanning rate is 0.2 mV s^{-1}, which suggests the excellent reversibility of the cells. The two pairs of redox peaks are located at 0.51/0.91 V and 0.80/1.01 V, respectively, which correspond to different intercalation and de-intercalation processes of Zn^{2+}.[31] As shown in Fig. 3b, the Zn//NVO-0.15C batteries deliver an initial specific capacity of 520.54 mA h g^{-1} at 0.2 A g^{-1}. They maintain a retention rate of 92.3% after 60 cycles. It is superior to those of NVO-0.1C (464.92 mA h g^{-1}), NVO (377.65 mA h g^{-1}), and NVO-0.2C electrodes (258.49 mA h g^{-1}). Fig. 3c shows the GCD curves for the first five charging and discharging processes of the Zn//NVO-0.15C cell at 0.2 A g^{-1}. The curves maintain a similar shape except for the first two cycles. This reveals that the activation process of the battery leads to a gradual increase in specific capacity. Besides, the curves manifest slightly inclined voltage platforms, which corresponds to the redox peaks of the CV curves.[32] This indicates that the embedding and de-embedding of Zn^{2+} in the cathode material are accompanied by the dynamic changes between V^{5+} and V^{4+}.

Rate capacity and cycle life are significant parameters to assess the comprehensive property of the cells. Fig. 3d indicates that the NVO-0.15C batteries deliver the specific capacity of 358.19 mA h g^{-1} at the current density of 5.0 A g^{-1}. They maintain a retention rate of 91% after 1000 cycles. From Fig. 3e, the NVO-0.15C cathodes present the specific capacities of 577.04, 533.05, 503.46, 480.33, 452.19, 425.4 and 378.21 mA h g^{-1} at 0.1, 0.2, 0.5, 1.0, 2.0, 3.0 and 5.0 A g^{-1}, respectively. When the current density restores to 0.1 A g^{-1}, the capacity returns to 525.69 mA h g^{-1}, which presents the retention rate of 91.1%. Compared with the other three devices, the NVO-0.15C cells present superior rate performance. The inserted chitosan provide high electrical conductivity and accelerate the migration rate of zinc ions. It facilitates the transfer of Zn^{2+}, which increase the specific capacity of batteries during charging and discharging. The GCD curves (Fig. 3f) indicate that the specific capacity decreases with the increase of the current

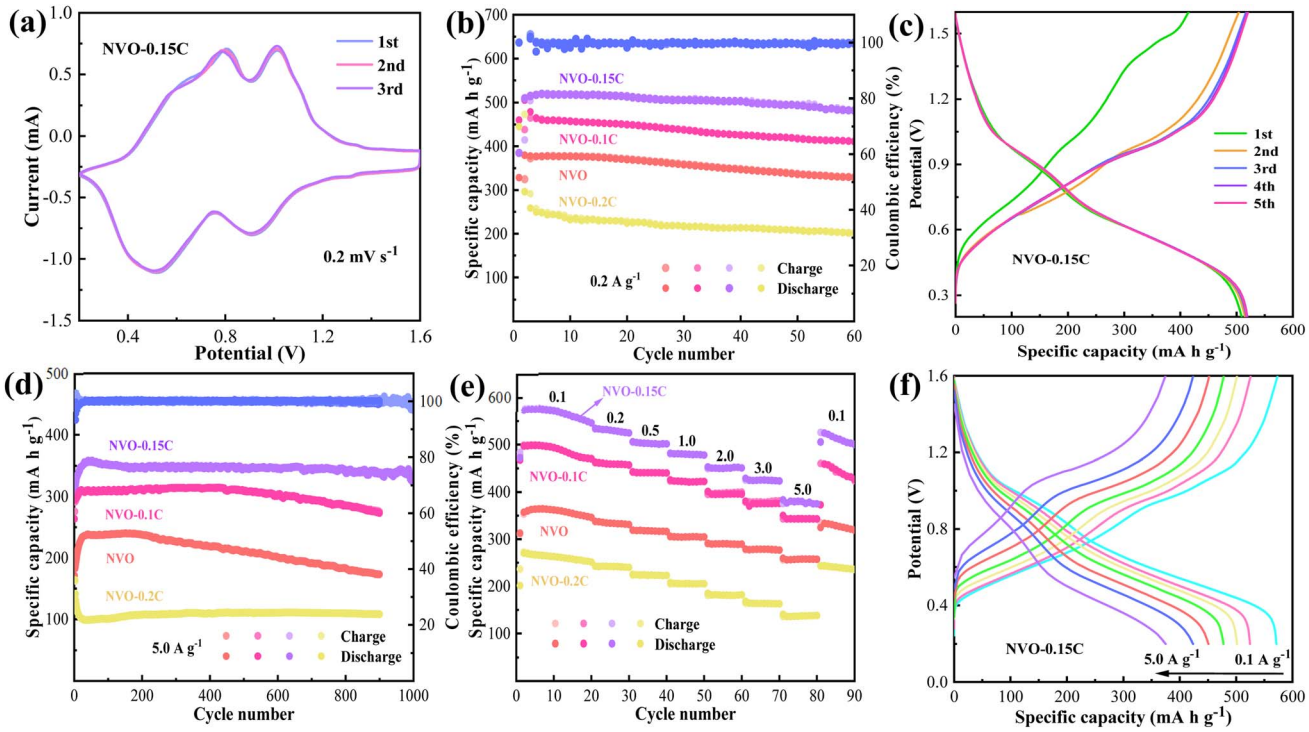

Fig. 3 Electrochemical performance (a) CV curves in the first 3 cycles at 0.2 mV s^{-1} (b) cycling performance at 0.2 A g^{-1} (c) GCD curves with various cycles at 0.2 A g^{-1} (d) long-term cycling performance at 5 A g^{-1} (e) rate capability at different current densities (f) GCD curves at various current densities.

density from 0.1 to 5.0 A g^{-1}. Besides, the curves present small charge–discharge platforms, which correspond to two pairs of redox peaks of the CV curves.

Subsequently, we investigate the electrochemical reaction kinetics of the Zn//NVO-0.15C batteries. Fig. 4a indicates the CV curves of the electrodes at various scanning speeds (0.2–1.0 mV s^{-1}). As the sweeping rates increase, the oxidation and reduction peaks shift to the different potential regions, indicating the occurrence of a polarization phenomenon. In addition, the entire areas of the CV curves gradually rise with the increment of the scanning speed, which reveals a multi-step intercalation and de-intercalation of Zn^{2+}.[33] The curves maintain their shapes in different sweep speeds, presenting the high reversibility of the cells. The relationship between scan rates (v) and current (i) is abided by eqn (1) as follows:[34]

$$i = av^b \quad (1)$$

where a and b are tunable parameters. The values of b are calculated by fitting the linear plot ($\log i$ *vs.* $\log v$). From Fig. 4b, the b values are in the range of 0.5–1 ($b_1 = 0.97$, $b_2 = 0.67$, $b_3 = 0.65$ and $b_4 = 0.66$). The result suggests that the surface and diffusion behaviors are synergistically regulate the charge and discharge process. In addition, the contribution rates of pseudocapacitive and diffusion are calculated *via* eqn (2) below:[35]

$$i(V) = k_1 v + k_2 v^{1/2} \quad (2)$$

where k_1 and k_2 are fixed constants. The $k_1 v$ and $k_2 v^{1/2}$ refer the capacitance and diffusion-controlled reactions, respectively. Fig. 4c suggests that the contribution ratio increases from 90.0% to 95.3%. It indicates that the pseudocapacitive behavior dominate the redox process as the scanning speeds increase. The GITT curves are further conducted to estimate the Zn^{2+} diffusion coefficient (D_{Zn}) of NVO-0.15C cathode. The D_{Zn} are calculated by the *e.g.* (3) as follows:[36]

$$D_{Zn} = \frac{4}{\pi\tau}\left(\frac{m_b v_m}{M_B S}\right)^2 \left(\frac{\Delta E_S}{\Delta E_\tau}\right)^2 \quad (3)$$

where τ is the current pulse time (s), m_b and M_B are the load mass of cathode (g) and the relative molecular mass (g mol^{-1}) of $NH_4V_4O_{10}$, respectively. v_m is the molar volume (cm^3 mol^{-1}). S is the total contact area of the cathode plate (cm^2). ΔE_s is the steady-state voltage change, due to the current pulse and ΔE_τ during the constant current pulse eliminates the iR drop. In Fig. 4d, the D_{Zn} values of the battery are between 10^{-6} and 10^{-8} cm^2 s^{-1} based on the curves during discharging. The high rate enhances fast transfer of Zn^{2+}.

Furthermore, EIS is employed to study the zinc storage behavior of Zn//NVO-0.15C cells, as shown Fig. 4e. The typical curve is composed of a semicircle and a line, where the area of semicircle represents the charge transfer resistance (R_{ct}). The inset is the schematic of the equivalent circuit. By fitting the curves, the assembled batteries using NVO, NVO-0.1C and NVO-0.2C materials manifest R_{ct} values of 37.21, 48.52 and 84.37 Ω, respectively. This indicates that the NVO-0.15C electrodes deliver the lower resistance (R_{ct} = 22.46 Ω) than other electrodes, which suggests the fast Zn^{2+} diffusion process within the cells. This is due to the intercalated chitosan enhances the electrical conductivity and widens the interlayer spacing. Besides, the large specific surface area and pore volume of NVO-

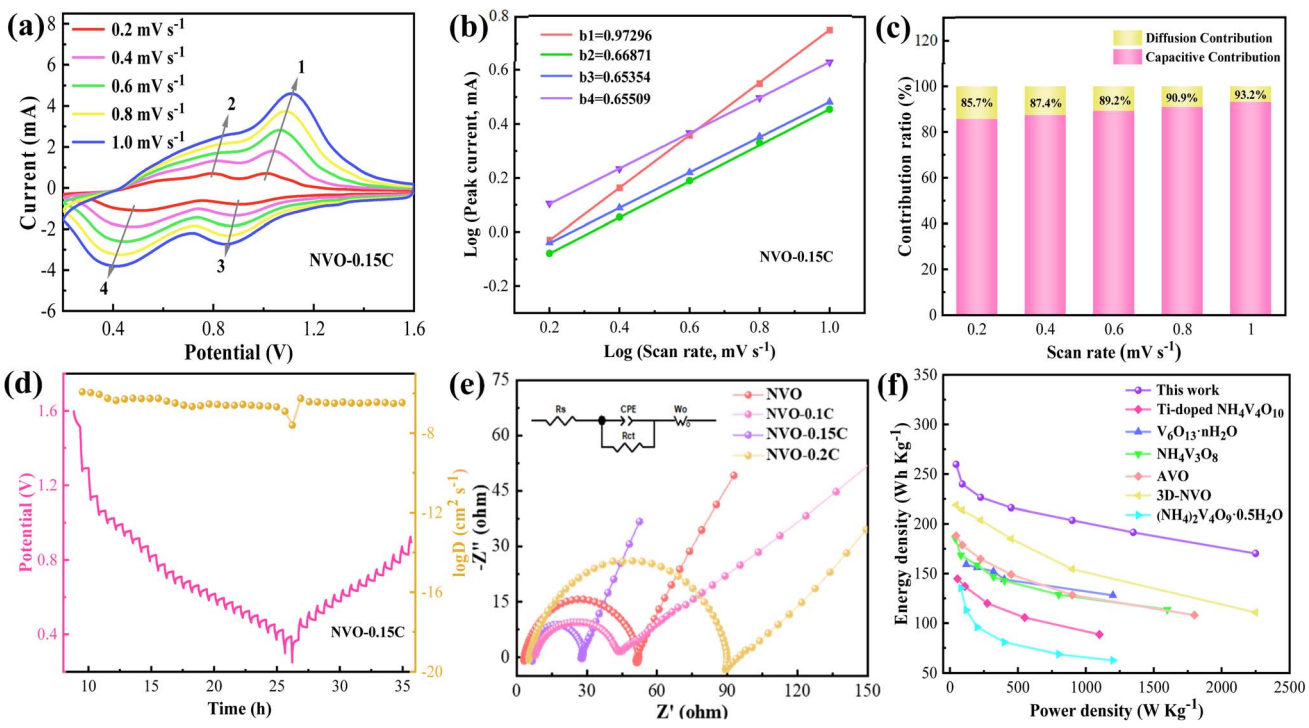

Fig. 4 Electrochemical reaction kinetics of the batteries (a) CV curves (b) the fitting plots of log(*i*) *versus* log(*v*) (c) capacitance contribution ratios at various scan rates (d) GITT curves (e) EIS plot (f) The ragone plot of various vanadate electrodes.

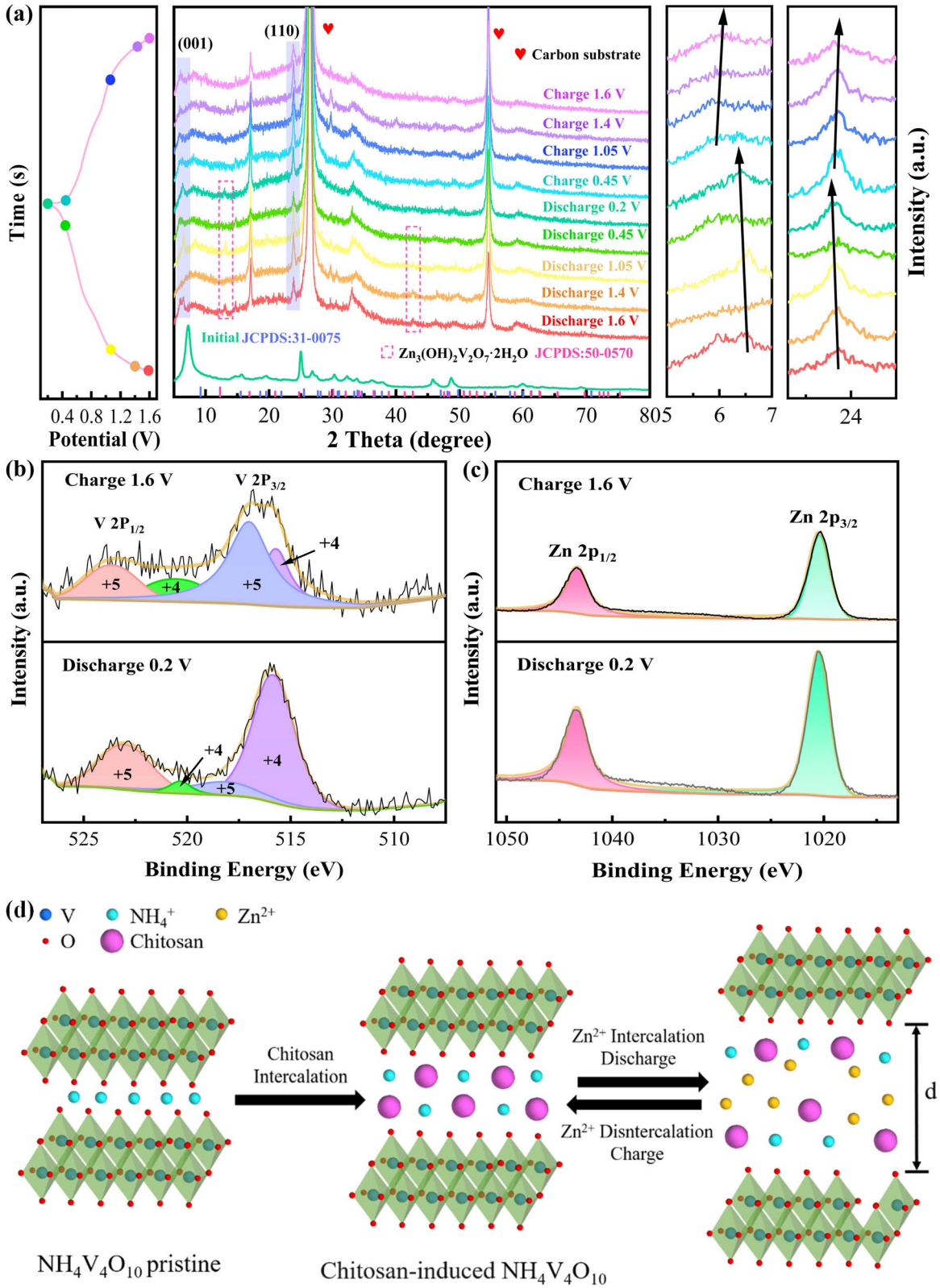

Fig. 5 Structural characterization (a) *exsitu* XRD at various charge and discharge states (b and c) XPS spectra of V and Zn in the full charging and discharging states (d) schematic diagram of the mechanism.

0.15C sample provide a wide distribution of Zn^{2+} storage sites. Energy density and power density are calculated by the equations as follows:[37]

$$E = QU/2m \quad (4)$$

$$P = IU/2m \quad (5)$$

where E (W h kg^{-1}) and P (W kg^{-1}) represent energy density and power density, respectively. I (A) signifies the discharge current, m (kg) is the loading mass of the cells. Q (A h) and U (V) refer to the capacity and operational voltage, respectively. The energy density of the assembled battery is 216.15 W h kg^{-1} at a power density of 450 W kg^{-1}. As shown in Fig. 4f, it is superior to some previously reported vanadate electrodes. This indicates that NVO-0.15C cathodes possess excellent zinc ion storage properties.

To investigate the Zn^{2+} storage mechanism of the cells, *ex situ* XRD is utilized to determine the structure evolution of the devices. Fig. 5a presents the XRD patterns of the samples during the second charge and discharge states. The intensities of these diffraction peaks increase with the enhanced discharge. The similar diffraction peaks in the initial and final states suggest the considerable reversibility of the crystal structure. The characteristic peaks do not apparently change except for the (001) and (110) planes due to the high intensities of carbon peaks. Owing to the contraction and expansion of the crystalline interstitial layers, the characteristic peaks reveal a slight movement toward different angles. During discharging, the characteristic peaks move to left due to the insertion of Zn^{2+}, which reveals the expansion of the interlayer space. On the contrary, the decrease of the layer spacing during charging leads the characteristic peaks move to right, which demonstrates the de-insertion of Zn^{2+}. Besides, the intercalated chitosan act as "pillars" between the $NH_4V_4O_{10}$ interlayers to maintain the layer structure. When charge to 1.6 V, the peak shapes and intensities of the pattern return to the initial state, indicating the superior reversibility during cycling. Moreover, it is notably that the signal peaks at 12.29 and 42.65° appear during discharge reaction, demonstrating the formation of $Zn_3(OH)_2V_2O_7\cdot 2H_2O$ phase (JCPDS no. 50-0570). During charging, the signal peaks gradually disappear, indicating the reversibility of the reaction. The detailed reaction is listed as follows:

$$V^{5+} + 4H_2O \rightarrow VO_2(OH)_2^- + 6H^+ \quad (6)$$

$$2VO_2(OH)_2^- + 3Zn^{2+} + 3H_2O \rightarrow Zn_3(OH)_2V_2O_7\cdot 2H_2O + 4H^+ \quad (7)$$

Finally, the *ex situ* XPS is also used to explore the composition and valence change of the NVO-0.15C samples. Fig. 5b shows the V 2p spectra in the charged and discharged states. V $2p_{1/2}$ and V $2p_{3/2}$ are V^{4+} and V^{5+} at 520.45/515.7 eV and 523.6/517.01 eV, respectively. The peak areas of the different valence states vary with the state of charge and discharge. During discharge process, the signal peak area of V^{5+} decrease accompanied by the increase of V^{4+}. The variation to the valence state of element V indicates the occurrence of reduction reaction and the insertion of Zn^{2+}. Then, the XPS shape is restored after charging, revealing the high reversibility. The two Zn 2p peaks in the charged state are located at 1043.26 eV (Zn $2p_{1/2}$) and 1020.44 eV (Zn $2p_{3/2}$), respectively, as shown in Fig. 5c. During the discharging, the increasing of the peak intensities confirms the embed of Zn^{2+} in the cathode. Fig. 5d further shows the mechanism of the NVO-0.15C cathode, confirming the reversible insertion of Zn^{2+} during charge and discharge.

4. Conclusions

In summary, we synthesized several $NH_4V_4O_{10}$ electrode materials by a simple hydrothermal strategy. The introduction of chitosan significantly enlarges the crystallographic spacing of the material and tailors the microscopic morphology of the samples. Moreover, the flower-like structure provides many active sites for the transfer of Zn^{2+} during electrochemical reaction. The assembled Zn//NVO-0.15C batteries possess an excellent specific capacity and long cycle life. It demonstrates potential application of the assembled cells in future high performance energy storage devices and systems. Simultaneously, this synthesis approach can be extended to prepare some other high-performance cathode materials for AZIBs.

Author contributions

Yaotong Li: conceptualization, methodology, data processing, and writing – original draft preparation. Chunru Zhao: software. Yaotong Li: visualization and investigation. Abdukayum Abdukader and Xiang Wu: validation, supervision, and writing – review & editing.

Conflicts of interest

The authors declare that they have no known competing financial interests.

References

1 Z. H. Yi, G. Y. Chen, F. Hou, L. Q. Wang and J. Liang, *Adv. Energy Mater.*, 2020, **11**, 2003065.
2 D. Selvakumaran, A. Q. Pan, S. Q. Liang and G. Z. Cao, *J. Mater. Chem. A*, 2019, **7**, 18209–18277.
3 V. Etacheri, R. Marom, R. Elazari, G. Salitra and D. Aurbach, *Energy Environ. Sci.*, 2011, **4**, 3243–3262.
4 Y. J. Wu, S. Wang, H. Li, L. Q. Chen and F. Wu, *InfoMat*, 2021, **3**, 827–853.
5 J. F. Peters, M. Baumann, B. Zimmermann, J. Braun and M. Weil, *Renewable Sustainable Energy Rev.*, 2017, **67**, 491–506.
6 N. Nitta, F. X. Wu, J. T. Lee and G. Yushin, *Mater. Today*, 2015, **18**, 252–264.
7 L. E. Blanc, D. Kundu and L. F. Nazar, *Joule*, 2020, **4**, 771–799.
8 M. Song, H. Tan, D. L. Chao and H. J. Fan, *Adv. Funct. Mater.*, 2018, **28**, 1802564.

9 Y. Tian, Y. L. An, C. L. Wei, B. J. Xi, S. L. Xiong, J. K. Feng and Y. T. Qian, *Adv. Energy Mater.*, 2021, **11**, 2002529.
10 X. H. Zheng, T. Ahmad and W. Chen, *Energy Storage Mater.*, 2021, **39**, 365–394.
11 Y. Liu, Y. Liu and X. Wu, *Batteries Supercaps*, 2023, **6**, e2200461.
12 Q. Yang, X. L. Li, Z. Chen, Z. D. Huang and C. Y. Zhi, *Acc. Mater. Res.*, 2022, **3**, 78–88.
13 C. Lu, Z. Yang, Y. J. Wang, Y. Zhang, H. Wu, Y. Guo and W. L. Cai, *Chin. Chem. Lett.*, 2023, **8**, 108572.
14 Y. Liu, Y. Liu and X. Wu, *Chin. Chem. Lett.*, 2023, **34**, 107839.
15 H. M. Jiang, Y. F. Zhang, L. Xu, Z. M. Gao, J. Q. Zheng, Q. S. Wang, C. G. Meng and J. Wang, *Chem. Eng. J.*, 2020, **382**, 122844.
16 Y. H. Dai, C. Y. Zhang, J. W. Li, X. Gao, P. Hu, C. M. Ye, H. Z. He, J. X. Zhu, W. Zhang, R. W. Chen, W. Zong, F. Guo, I. P. Parkin, D. J. L. Brett, P. R. Shearing, L. Q. Mai and G. J. He, *Adv. Mater.*, 2024, 2310645.
17 L. Zhang, X. H. Qin, L. Wang, Z. F. Zhao, L. W. Mi and Q. Q. Lu, *Front. Chem. Sci. Eng.*, 2023, **17**, 1244–1253.
18 Y. Liu, Y. Liu, X. Wu and Y. R. Cho, *ACS Appl. Mater. Interfaces*, 2022, **14**, 11654–11662.
19 S. J. Li, X. Y. Xu, W. X. Chen, J. W. Zhao, K. Wang, J. S. Shen, X. Chen, X. Lu, X. X. Jiao, Y. Y. Liu and Y. Bai, *Energy Storage Mater.*, 2024, **65**, 103108.
20 M. Zhao, S. L. Li, X. Wu and S. H. Luo, *Adv. Mater. Technol.*, 2024, **9**, 2400125.
21 C. R. Zhao, Y. Liu, X. Wu and S. H. Luo, *Adv. Sustainable Syst.*, 2024, **8**, 2400077.
22 Y. Q. Peng, L. Mo, T. T. Wei, Y. F. Wang, X. X. Zhang, Z. Q. Li, Y. Huang, G. Yang and L. H. Hu, *Small*, 2023, **19**, 2306972.
23 K. X. Li, Y. Liu and X. Wu, *CrystEngComm*, 2022, **24**, 5421.
24 H. Tang, F. Y. Chao, H. Y. Luo, K. S. Yu, J. Wang, H. B. Chen, R. M. Jia, F. Y. Xiong, Y. Q. Pi, P. Luo and Q. Y. An, *ChemSusChem*, 2023, **15**, e202300403.
25 X. X. Cai, Y. Zhang, H. H. Cheng, C. F. Liu, Z. W. Wang, H. Ye, Y. L. Pan, D. Z. Jia and H. Lin, *Small*, 2023, **19**, 2304668.
26 Q. F. Li, X. H. Rui, D. Chen, Y. Z. Feng, N. X, L. Y. Gan, Q. Zhang, Y. Yu and S. M. Huang, *Nano-Micro Lett.*, 2020, **12**, 67–78.
27 W. Yang, L. B. Dong, W. Yang, C. J. Xu, G. J. Shao and G. X. Wang, *Small Methods*, 2020, **4**, 1900670.
28 T. Y. Wei, Y. Y. Liu, G. Z. Yang and C. X. Wang, *Energy Storage Mater.*, 2020, **30**, 130–137.
29 R. Sun, Z. X. Qin, X. L. Liu, C. H. Wang, S. J. Lu, Y. F. Zhang and H. S. Fan, *ACS Sustainable Chem. Eng.*, 2021, **35**, 11769–11777.
30 Y. Liu and X. Wu, *J. Energy Chem.*, 2023, **87**, 334–341.
31 H. Luo, B. Wang, C. L. Wang, F. D. Wu, F. D. Jin, B. W. Cong, Y. Ning, Y. Zhou, D. L. Wang, H. K. Liu and S. X. Dou, *Energy Storage Mater.*, 2020, **33**, 390–398.
32 G. Z. Yang, T. Y. Wei and C. X. Wang, *ACS Appl. Mater. Interfaces*, 2018, **10**, 35079–35089.
33 Y. Liu, Y. Liu and X. Wu, *ACS Sustainable Chem. Eng.*, 2023, **11**, 13298–13305.
34 N. Zhang, Y. Dong, M. Jia, X. Bian, Y. Y. Wang, M. D. Qiu, J. Z. Xu, Y. C. Liu, L. F. Jiao and F. Y. Cheng, *ACS Energy Lett.*, 2018, **3**, 1366–1372.
35 S. Wu, Y. F. Wang, W. L. Liu, M. M. Ren, F. G. Kong, S. J. Wang, X. Q. Wang, H. Zhao and J. M. Bao, *Inorg. Chem. Front.*, 2018, **5**, 3067–3073.
36 Y. Liu, Y. Liu, X. Wu and Y. Cho, *J. Colloid Interface Sci.*, 2022, **628**, 33–40.
37 W. Zhang, Y. Xiao, C. Zuo, W. Tang, G. Liu, S. Wang, W. Cai, S. Dong and P. Luo, *ChemSusChem*, 2021, **14**, 971.